Mesoscopic current transport in two-dimensional materials with grain boundaries: Four-point probe resistance and Hall effect

Lotz, Mikkel Rønne; Boll, Mads; Østerberg, Frederik Westergaard; Hansen, Ole; Petersen, Dirch Hjorth

Published in:
Journal of Applied Physics

Link to article, DOI:
10.1063/1.4963719

Publication date:
2016

Document Version
Publisher's PDF, also known as Version of record

Mesoscopic current transport in two-dimensional materials with grain boundaries: Four-point probe resistance and Hall effect

Mikkel R. Lotz, Mads Boll, Frederik W. Østerberg, Ole Hansen, and Dirch H. Petersen

Citation: Journal of Applied Physics **120**, 134303 (2016); doi: 10.1063/1.4963719
View online: http://dx.doi.org/10.1063/1.4963719
View Table of Contents: http://scitation.aip.org/content/aip/journal/jap/120/13?ver=pdfcov
Published by the AIP Publishing

Mesoscopic current transport in two-dimensional materials with grain boundaries: Four-point probe resistance and Hall effect

Mikkel R. Lotz,[1] Mads Boll,[1,2] Frederik W. Østerberg,[1,3] Ole Hansen,[1,4] and Dirch H. Petersen[1,a)]

[1]*Department of Micro- and Nanotechnology, Technical University of Denmark, DTU Nanotech Building 345 East, DK-2800 Kgs. Lyngby, Denmark*
[2]*Department of Physics, Technical University of Denmark, DTU Physics Building 309, DK-2800 Kgs. Lyngby, Denmark*
[3]*CAPRES A/S, Scion-DTU, Building 373, DK-2800 Kgs. Lyngby, Denmark*
[4]*Danish National Research Foundation's Center for Individual Nanoparticle Functionality (CINF), Technical University of Denmark, DK-2800 Kgs. Lyngby, Denmark*

(Received 28 April 2016; accepted 15 September 2016; published online 3 October 2016)

We have studied the behavior of micro four-point probe (M4PP) measurements on two-dimensional (2D) sheets composed of grains of varying size and grain boundary resistivity by Monte Carlo based finite element (FE) modelling. The 2D sheet of the FE model was constructed using Voronoi tessellation to emulate a polycrystalline sheet, and a square sample was cut from the tessellated surface. Four-point resistances and Hall effect signals were calculated for a probe placed in the center of the square sample as a function of grain density n and grain boundary resistivity ρ_{GB}. We find that the dual configuration sheet resistance as well as the resistance measured between opposing edges of the square sample have a simple unique dependency on the dimension-less parameter $\sqrt{n}\rho_{GB}G_0$, where G_0 is the sheet conductance of a grain. The value of the ratio R_A/R_B between resistances measured in A- and B-configurations depends on the dimensionality of the current transport (i.e., one- or two-dimensional). At low grain density or low grain boundary resistivity, two-dimensional transport is observed. In contrast, at moderate grain density and high grain resistivity, one-dimensional transport is seen. Ultimately, this affects how measurements on defective systems should be interpreted in order to extract relevant sample parameters. The Hall effect response in all M4PP configurations was only significant for moderate grain densities and fairly large grain boundary resistivity. *Published by AIP Publishing.* [http://dx.doi.org/10.1063/1.4963719]

I. INTRODUCTION

The seminal work on graphene[1] has fueled a strong interest into synthesis, characterization, and application of graphene as well as other two-dimensional (2D) materials. However, commercialization of graphene based applications decidedly calls for the development of reliable methods of producing high quality graphene and non-destructive methods to electrically characterize it.[2] Synthesis of graphene using chemical vapor deposition (CVD) has shown great promise,[3,4] yet still contains a wide range of defects compared to its mechanically exfoliated counterpart. These defects include vacancies, physi- or chemisorbed adatoms, lattice imperfections, substitutional atoms, and electron-hole puddles as well as extended defects which include folds, cracks, and grain boundaries (GBs). GBs are presently ubiquitous in CVD processed material since the technique relies on stitching together—initially separate—grains in order to achieve larger coherent sheets.[5] Both theoretical[6,7] and experimental studies[8,9] on transport through graphene GBs found that GBs cause potential barriers for the carrier transport and result in an increase in resistance, which sometimes is 30 times larger than the bulk graphene resistance at the center of the grain.[10–12] Thus, the GBs are significantly deteriorating the electrical properties of the films, which in turn affect the performance of graphene based devices, e.g., field-effect transistors.[13]

Micro four-point probe (M4PP) metrology has previously been used for non-destructive electrical characterization of graphene films.[14] M4PP metrology can be used to measure the sheet resistance (or sheet conductance), and in addition, the method allows for extraction and evaluation of geometry related parameters such as the resistance ratio[15,16] and the Hall effect signal caused by the Lorentz force.[17]

In previous work,[18] we developed a finite element (FE) model to investigate how the M4PP signature differs for measurements on 2D and quasi-1D materials; these signatures had already been observed experimentally.[15,16] We successfully validated the FE approach by comparing calculations for a single line defect to the analytical result.[19] The model was limited in its scope since only samples with insulating line defects were studied, which may be a reasonable representation of 2D materials in which current transport is dominated by transfer defects such as rips and tears. However, with improvements in fabrication of 2D materials, today transfer defects can now often be neglected. The FE model proposed here is well suited for simulating M4PP measurements on 2D materials fabricated by chemical vapor deposition in which current transport is dominated by intra-grain conductance and domain boundary resistance. The

a)Electronic mail: dirch.petersen@nanotech.dtu.dk.

model is also more comprehensive than the previous one, as it also includes an applied magnetic field such that Hall effects can also be extracted. The model is coupled with a Monte Carlo approach so that an unbiased correlation between surface composition and the parameters extracted from the M4PP measurement can be studied.

We begin our study by defining the four-point notation we use and a detailed description of the FE model. Then, we continue to examine the simulation results by comparing the effective sheet conductances obtained from M4PP and a square electrode setup, which are shown to largely agree and follow a predicted dependency on grain boundary resistivity and grain density. We proceed to study the distribution of simulated R_A/R_B ratio as grain boundary resistivity and grain density are varied, from where it becomes apparent how important the relative grain size to probe pitch is in affecting the dimensionality of the current transport. Finally, we study the effect of grain boundary resistivity and grain density on the magnitude and distribution of the Hall signal.

II. FOUR-POINT PROBE DEFINITIONS

A four-point probe has 24 possible electrode configurations, 18 of which can be disregarded as they arrive from trivial interchanging of current direction and/or potential pins. The three remaining configurations in addition to their conjugate configurations (where the current pins and voltage potential pins are interchanged) make up what is known as the electrode configurations A, B, and C (A′, B′, and C′ for their respective conjugate configurations). In the A configuration, the current is applied between pins no. 1 and 4 (pin labels for the collinear four-point probe are illustrated in Fig. 1), while the electrical potential is measured between pins no. 2 and 3 such that the resistance becomes $R_A = V_{23}/I_{14}$. In the B configuration, the current is sourced between pins no. 1 and 3, while pins no. 2 and 4 measure the electrical potential ($R_B = V_{24}/I_{13}$), and finally, in the C configuration, pins no. 1 and 2 apply the current while pins no. 3 and 4 measure the potential ($R_C = V_{43}/I_{12}$). The conjugate configurations are found by interchanging current-carrying pins with the voltage-sensing pins.

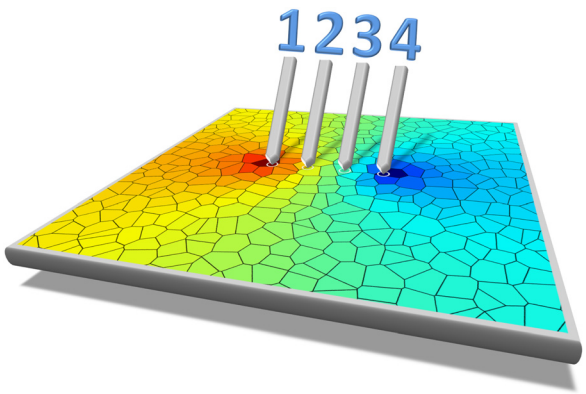

FIG. 1. Illustration of an M4PP probing a surface comprised grains and GBs. The surface colormap shows the magnitude of the electrical potential with the probe in its A configuration. The four probe pins are distinguished by labels (1–4).

It is convenient to define the average resistance, $\bar{R}_i = (R_i + R_{i'})/2$, and resistance difference, $\Delta R_i = R_i - R_{i'}$, and where $i \in \mathrm{A}, \mathrm{B}, \mathrm{C}$. The Hall effect signal ΔR_i is proportional to the Hall sheet resistance R_H and is affected by the geometry, i.e., the proximity of boundaries obstructing current transport. The average resistance $\bar{R}_i$ depends on the sheet resistance including geometrical magnetoresistance.[17]

For a sample with a highly non-uniform conductance and samples that are not simply connected, it is furthermore convenient to redefine the configuration resistances such that

$$\bar{R}_{\tilde{\mathrm{A}}} \equiv \max(|\bar{R}_i|)\ ,\ \bar{R}_{\tilde{\mathrm{C}}} \equiv \min(|\bar{R}_i|)\ ,\ \bar{R}_{\tilde{\mathrm{B}}} \equiv \bar{R}_{\tilde{\mathrm{A}}} - \bar{R}_{\tilde{\mathrm{C}}}.$$

This definition ensures that a dual configuration van der Pauw conductance always can be found and it limits the modified resistance ratio to the closed interval $\bar{R}_{\tilde{\mathrm{A}}}/\bar{R}_{\tilde{\mathrm{B}}} \in [1;2]$, as opposed to $\bar{R}_\mathrm{A}/\bar{R}_\mathrm{B} \in]-\infty;\infty[$. The redefinition of configurations only matters in the event of highly non-uniform samples, e.g., in the presence of a large number of insulating defects in proximity of the electrodes. In such cases, either of the resistance ratios $\bar{R}_\mathrm{A}/\bar{R}_\mathrm{B}$, $\bar{R}_\mathrm{A}/\bar{R}_\mathrm{C}$ or $\bar{R}_\mathrm{B}/\bar{R}_\mathrm{C}$ could become unity. With the configuration redefinition, $\bar{R}_{\tilde{\mathrm{A}}}/\bar{R}_{\tilde{\mathrm{B}}}$ will itself become unity in cases where any of the values $|\bar{R}_\mathrm{A}|$, $|\bar{R}_\mathrm{B}|$ or $|\bar{R}_\mathrm{C}|$ approaches zero.

The van der Pauw equation for collinear four-point probes in terms of the redefined configurations becomes[20]

$$\exp(2\pi\bar{R}_{\tilde{\mathrm{A}}}\tilde{G}_\mathrm{s}) - \exp(2\pi\bar{R}_{\tilde{\mathrm{B}}}\tilde{G}_\mathrm{s}) = 1, \qquad (1)$$

which relates the average measured resistances in the $\tilde{\mathrm{A}}$ and $\tilde{\mathrm{B}}$ configurations to an apparent sheet conductance $\tilde{G}_\mathrm{s}$, which in case of a perfect sample equals the effective sheet conductance G_s and also the internal grain sheet conductance G_0. Note that Eq. (1) is not valid in the case where $\bar{R}_{\tilde{\mathrm{A}}}/\bar{R}_{\tilde{\mathrm{B}}} = 1$ (1D conduction).

III. FINITE ELEMENT MODEL

The FE model was assembled in COMSOL Multiphysics 5.1 using the "ACDC" physics-module and includes a 10*s*-by-10*s* 2D film (*s* is the probe pitch) with an M4PP at its center as illustrated by the example in Fig. 1. The relatively small size of our model ensured a fairly short simulation time with the trade-off being that for the case of a perfect 2D conductor (no defects) $\bar{R}_{\tilde{\mathrm{A}}}/\bar{R}_{\tilde{\mathrm{B}}} = 1.2079$, instead of its well-known value on an infinite, perfect sample; $\bar{R}_{\tilde{\mathrm{A}}}/\bar{R}_{\tilde{\mathrm{B}}} = \ln(4)/\ln(3) \simeq 1.2619$.[15]

The FE model consists of multiple components, as visualized by the simulation layout shown in Fig. 2. The black dots represent the seeds from which the 2D film was tessellated using a Voronoi diagram,[21] thus partitioning it into cells that closely resemble grains grown in a CVD process. At the beginning of each simulation, the seeds were initially distributed in a regular grid with one seed at each grid point, and subsequently, a random displacement in the *x*- and *y*-directions, with a maximum displacement of half the grid spacing, was added to each seed point. This seed layout ensured that the grain density, *n*, accurately reflects the simulated system both globally and locally. The shaded square at the center of the model encloses the area included in the simulation. From one simulation to the next, the position of the

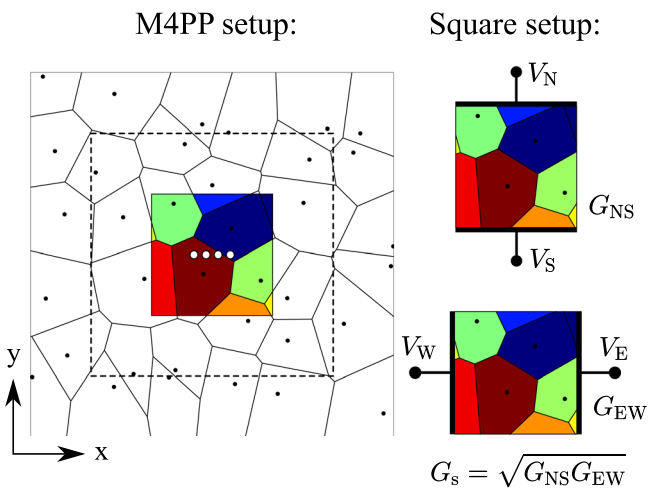

FIG. 2. Sketch of the FE model and the two measurement setups used. The black dots represent seeds from which the Voronoi tessellation is drawn. The shaded square at the center shows the part of the tessellated surface included in the simulation. The dashed line outlines the area that the shaded square can occupy by shifting its position. In the M4PP setup (left), the four white dots at the center of the shaded square show the locations of the four probe pins. In the square setup (right), the effective sheet conductance G_s was calculated as the geometric mean of conductances found in the two configurations, NS and EW, respectively, given by $G_i = I_i/V_i$, where $i \in \mathrm{NS}, \mathrm{EW}$.

shaded square shifted randomly within the area outlined by the dashed line. This was done in order to obtain a higher degree of randomness between each simulated system and to avoid slight grain density deviations inherent to the Voronoi tessellation when approaching the boundary of the seeded region (outlined by the black rim); this was particularly important in low grain density systems. At the center of the shaded square, four equally spaced white dots show the positions of the four probe pins. This symmetric position of the M4PP ensures that in the case of a perfect uniform film, dual configuration measurements yield the sheet conductance of the material,[22] i.e., $\tilde{G}_s = G_0$ and that the Hall signals vanish,[17] i.e., $\Delta R_i = 0$.

In addition to M4PP measurement calculations, the model was also adapted to allow calculations of the effective sheet conductance as illustrated in Fig. 2 (right). The conductances between iso-potential electrodes on opposing sides of the square sample, G_{NS} and G_{EW}, were calculated for the two configurations shown, and the geometric mean reported as the effective sheet conductance G_s.[23,24]

Initially, a coarse triangular mesh was applied; then two adaptive mesh refinement steps followed to optimize the mesh by increasing the mesh resolution in locations with large potential gradients, such as close to the current inlets. As shown in our previous publication,[18] two mesh-refinement steps were sufficient to ensure a relative error of less than 1% of the fully converged solution. For questions concerning the validity of this method of modelling M4PP measurements, we also refer to a previous publication, Ref. 19, where simulations on a simple system containing just a single line defect were compared to the analytical result.

A. Calculations

For each Voronoi tessellation with a given grain density n, square samples of $10 \times 10s^2$ were cut and M4PP resistances for all 6 configurations, A, B, C, A′, B′ and C′, calculated for each setting of the grain boundary resistivity. The sheet resistance of a single grain was kept at $R_0 \simeq 1/G_0 = 1\,\Omega$, which defines the resistance scale used. Note, the specific value of R_0 is irrelevant; however, in order to simulate the problem numerically, we have to assign a value to it.

The grain boundary resistivity, ρ_{GB} (unit Ω m), was scaled in units of $R_0 s$, since we have chosen the probe pitch s as the length scale in our calculations. In the calculations, we have studied grain boundary resistivities in a range of six orders of magnitude, from almost completely transparent ($\rho_{GB}G_0 s^{-1} = 10^{-3}$) to almost completely insulating ($\rho_{GB}G_0 s^{-1} = 10^{3}$). By transparent, we signify that current passes the boundary with an insignificant potential drop.

Hall effect was included in the calculations by specifying the two-dimensional conductance tensor of the material; the diagonal elements were set to $G_0 = 1$ S as explained above, while the off diagonal elements were set to $\pm G_H$ with $G_H = G_0\mu_H B_z$, where μ_H is the Hall mobility and B_z is the magnetic flux density normal to the surface. In the calculations, the product of Hall mobility and magnetic flux density was fixed at $\mu_H B_z = 0.01$. A relatively small value of $\mu_H B_z$ was chosen to minimize the magnetoresistance effect, which could complicate interpretation of the results. It follows that the Hall sheet resistance becomes $R_H \simeq 0.01\,\Omega$.

IV. RESULTS

A. Effective sheet conductance

The effective sheet conductance G_s is the most important parameter in many applications, and it is therefore important to see how G_s varies with grain density and GB resistivity; both when G_s is extracted from M4PP measurements and when measured on a square sample with source and drain electrodes on opposing sides.

Consider a rectangular resistor sample of length L and width W, which is completely filled with identical square grains of density n. In this resistor, intra-grain transport contributes $R_0 L/W$ to the total effective sheet resistance, while the current has to pass $L\sqrt{n}$ grain boundaries of width W, and therefore, the grain boundaries contribute $(\rho_{GB}/W)L\sqrt{n}$ to the total effective sheet resistance, which then becomes $R_s = (R_0 + \rho_{GB}\sqrt{n})L/W$, reminiscent of the expression given in Ref. 9. It follows that the expected effective sheet conductance normalized to the intra grain sheet conductance becomes

$$\frac{G_s}{G_0} = \frac{1}{1 + \sqrt{n}\rho_{GB}G_0}, \tag{2}$$

and thus depends only on a single dimension-less parameter $\sqrt{n}\rho_{GB}G_0$. Even though the equation is derived under these very simplified conditions, we are of the opinion that it has a more general validity; however, we have not yet found any analytical proof.

Figure 3 shows the mean normalized apparent sheet conductance calculated using Eq. (1) for the M4PP as well as the mean effective sheet conductance calculated for a square setup. The sheet conductance data are shown as a function of the dimension-less parameter $\sqrt{n}\rho_{GB}G_0$ representing large

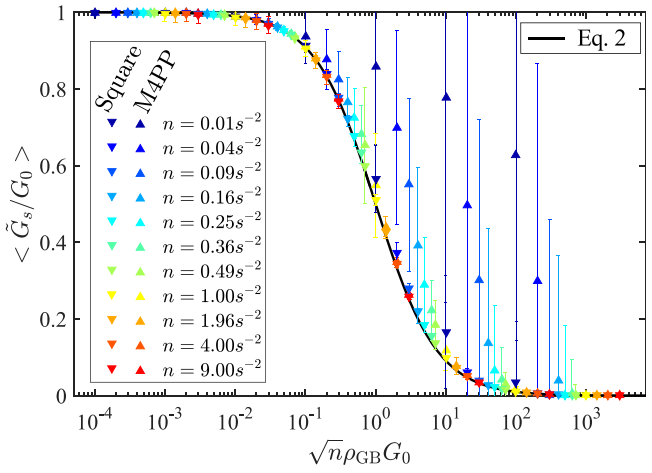

FIG. 3. Mean normalized sheet conductance, calculated using Eq. (1), and its standard deviation (error bars) based on data collected from randomly constructed M4PP and square setup simulations. It illustrates how both models tend to yield values that closely resemble the analytical model (solid black line), with the exception of M4PP measurements of samples with low grain density, $n \leq 0.25s^{-2}$.

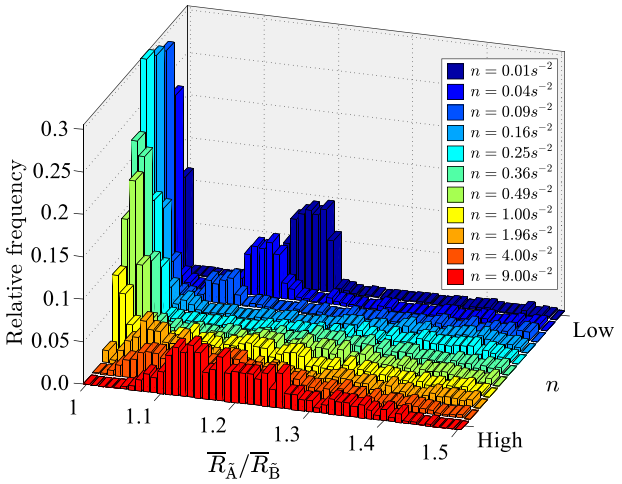

FIG. 4. Histogram of the calculated resistance ratio $\bar{R}_{\tilde{A}}/\bar{R}_{\tilde{B}}$ collected from randomly constructed simulations as a function of grain density n, with almost insulating grain boundaries ($\rho_{GB}G_0s^{-1} = 10$). The axis labels "Low" ($n = 0.01s^{-2}$) and "High" ($n = 9s^{-2}$) signify the two extremes in grain density relative to the electrode pitch squared.

variations in both grain density n and GB resistivity ρ_{GB}. We see that the majority of the mean sheet conductance data follows a single unique curve in perfect agreement with Eq. (2). For low grain density systems, $n = [0.01s^{-2}; 0.25s^{-2}]$, the four-point measurements are expected to deviate from the analytical model, Eq. (2), as the M4PP is likely to measure either within a single grain or across a single grain boundary giving rise to extreme values.

In the square setup, this is less likely to occur since the distance between electrodes is much larger ($10 \times 10s^2$); this explains why a similar deviation is not observed for the square setup, i.e., the measured conductance is averaged over a larger number of GBs and is given as the geometric mean of NS and EW configurations as illustrated in Fig. 2. The fact that data points from the square setup and M4PP data points are almost identical show that the M4PP on average actually measures the effective sheet conductance even on samples with a high grain boundary density.

B. Resistance ratio distribution

The resistance ratio $\bar{R}_{\tilde{A}}/\bar{R}_{\tilde{B}}$ has previously been shown to assume values that differ significantly between 2D and quasi-1D materials,[15,18,19] and here, we study the distribution on the grainy material.

The histogram in Fig. 4 shows the distribution of the calculated resistance ratios as a function of the grain density for samples with weakly conductive grain boundaries ($\rho_{GB}G_0s^{-1} = 10$). The figure neatly captures the transitions between 2D conductance at low grain density, e.g., $n = 0.01s^{-2}$, quasi-1D at moderate grain density, e.g., $n = 0.25s^{-2}$, and 2D conductance again at high grain density, e.g., $n = 9s^{-2}$. At $n = 0.01s^{-2}$, only about 12% of the simulations yield $\bar{R}_{\tilde{A}}/\bar{R}_{\tilde{B}} = [1.0; 1.03]$, identified here as a quasi-1D measurement signature.[15] As the grain density increases, the fraction of 1D measurement signatures, i.e., $\bar{R}_{\tilde{A}}/\bar{R}_{\tilde{B}} = [1.0; 1.03]$, increases to ~50% at $n = 0.25s^{-2}$ and $n = 0.36s^{-2}$. Hereafter, the fraction of 1D signatures rapidly declines until $n = 9s^{-2}$, at which point remarkably none of the simulations registered as quasi-1D signatures. Initially puzzled by this observed behavior at high densities, we soon arrived at the conclusion that this was likely caused by a reduction in the probability of having two pins isolated on the same grain. This also explains why we see a peak at $n = 0.25s^{-2}$ and $n = 0.36s^{-2}$, as this is where this probability is at its highest. When considering that in the limit of extremely high grain densities, the sample essentially becomes 2D-like again albeit with a lower overall sheet conductance, this observed behavior of the resistance ratio distribution re-approaching its 2D signature form, makes perfect sense. It is very clear from this argument that the relative grain size to probe pitch plays a decisive role in determining the $\bar{R}_{\tilde{A}}/\bar{R}_{\tilde{B}}$ outcome of an M4PP measurement.

Having initially focussed on comparing simulations with a constant grain boundary resistivity of $\rho_{GB}G_0s^{-1} = 10$, we now take a look at how the outcome of the simulations are affected when changing the grain boundary resistivity from almost insulating to almost transparent. Figure 5 shows histograms of resistance ratios as a function of normalized grain boundary resistivity ($\rho_{GB}G_0s^{-1}$) for two grain densities, (a) $n = 0.49s^{-2}$ and (b) $n = 9.00s^{-2}$. At low grain boundary resistivity, we observe a distinct peak around $\bar{R}_{\tilde{A}}/\bar{R}_{\tilde{B}} = 1.2079$ at both densities; we recognize this as the familiar 2D signature for the $10 \times 10s^2$ sample. The peak soon disappears when $\rho_{GB}G_0s^{-1}$ is increased, and then, we start to see a difference in behavior between the two grain densities. In Fig. 5(a) for high values of $\rho_{GB}G_0s^{-1}$, a new distribution peak emerges at $\bar{R}_{\tilde{A}}/\bar{R}_{\tilde{B}} = 1.0$, this is known as the 1D signature peak, while in Fig. 5(b), we see a broadening of the original 2D signature peak until distinct peaks are completely absent in the histogram. From this observation, we infer that the range of attainable values of $\bar{R}_{\tilde{A}}/\bar{R}_{\tilde{B}}$ is highly dependent on both the grain size and the degree to which the GBs disturb the transport of electrons in the measured film. Note also how $\bar{R}_{\tilde{A}}/\bar{R}_{\tilde{B}} = 1.2079$ is not a unique value exclusively reserved for $10 \times 10s^2$ 2D conductors, since we observe many simulations with this value even on material with grain

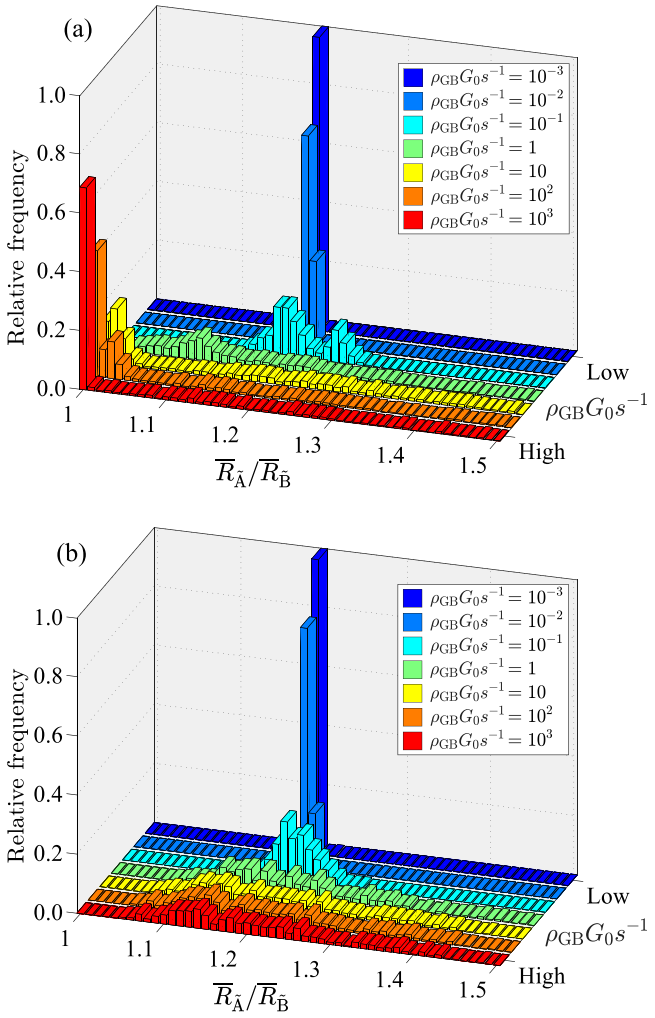

FIG. 5. Histograms of the calculated resistance ratio $\bar{R}_{\tilde{A}}/\bar{R}_{\tilde{B}}$ collected from randomly constructed simulations as a function of normalized grain boundary resistivity, with a grain density of (a) $n = 0.49s^{-2}$ and (b) $n = 9.00s^{-2}$. The axis labels "Low" ($\rho_{GB}G_0s^{-1} = 10^{-3}$) and "High" ($\rho_{GB}G_0s^{-1} = 10^{3}$) signify the two extremes in normalized grain boundary resistivity (dimension-less).

boundaries and a current flow pattern that is clearly not in accordance with a 2D conductor. We therefore infer that a single measurement provides insufficient information to ascertain electrical continuity of the sample; instead, a significant number of measurements must be used and their distribution analyzed to see if the values are centered closely around the expected resistance ratio for the 2D conductor.

C. Hall effect signal

In a sample free of insulating boundaries and defects, the Hall effect signal is exactly zero in all possible electrode configurations with the symmetric arrangement of the electrodes used here. A Hall effect signal is, however, expected when current rotation (induced by the Lorentz force in a magnetic field) is suppressed by nearby insulating boundaries such as extended defects or partially insulating grain boundaries. In micro Hall effect measurements, the B-configuration gives the largest Hall signal when the collinear four-point probe is placed in proximity to a parallel boundary. The maximum possible magnitude of the Hall effect signals is $\max(|\Delta R_i|) = 2R_H$, i.e., it can take any value between $-2R_H$ and $2R_H$.[17] It follows that the presence of a Hall effect signal is therefore also an indication of a defective material.

Since the geometrical arrangement of grain boundaries in proximity of the M4PP is equally likely to produce positive or negative Hall effect signals, the mean Hall effect signal is expected to be zero for any set of grain boundary resistivity and grain density. We therefore use the normalized standard deviation of the Hall effect signal $\sigma(\Delta R_i/2R_H)$ to represent the Hall effect response to sample parameters.

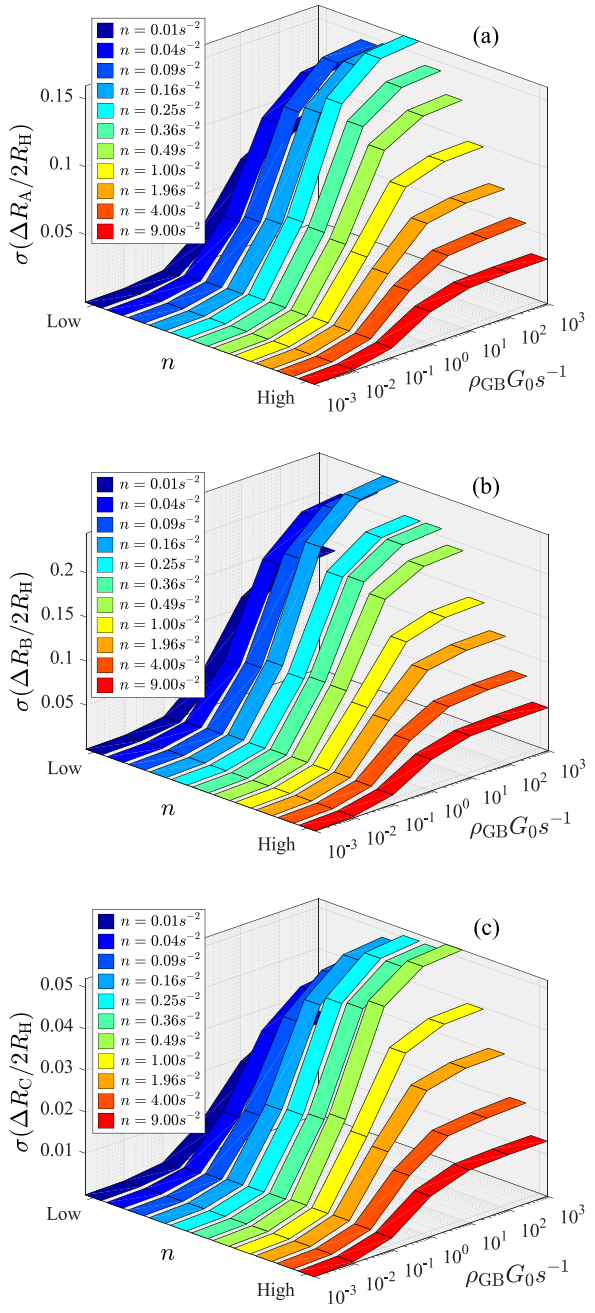

FIG. 6. Ribbon plots of the normalized standard deviation of the Hall effect signal measured in (a) the A-configuration, (b) the B-configuration, and (c) the C-configuration. The data are results from running randomly constructed simulations for each grain density n and then sweeping across the range of GB resistivities $\rho_{GB}G_0s^{-1}$. The axis labels "Low" ($n = 0.01s^{-2}$) and "High" ($n = 9s^{-2}$) signify the two extremes in grain density relative to the electrode pitch squared.

Figures 6(a)–6(c) show the standard deviations of the normalized Hall effect signals in the A-, B-, and C-configurations, respectively. All three graphs show common trends: At low grain boundary resistivity (electron transparent grain boundaries), the Hall effect signals vanish regardless of the grain density. At high grain boundary resistivity (almost insulating grain boundaries), a significant Hall effect signal appears for moderate grain densities, and with the largest amplitude for grain densities in the range $n = 0.09s^{-2}$ to $n = 0.49s^{-2}$. The magnitude of the Hall effect signal decays towards lower as well as higher grain densities. The decay in signal magnitude towards lower grain density was expected, since perfect material has zero Hall effect response. The decaying signal magnitude towards higher grain densities may be explained as a result of increasing symmetry in the geometrical arrangement of grain boundaries in vicinity of the probe as the grain density is increased. Finally, we note that the standard deviation of the Hall signal is larger in the B-configuration and smaller in the C-configuration.

V. CONCLUSION

Our FE model calculations have shown that dual configuration M4PP measurements indeed measure the effective sheet resistance of poly-crystalline 2D sheets, regardless of the grain boundary resistivity and grain density. The effective sheet resistance was, using the "defining" square setup, shown to depend on a single dimension-less parameter $\sqrt{n}\rho_{GB}G_0$. However, the standard deviation of the M4PP sheet resistance measurement can become quite large on low grain density samples.

The resistance ratio $\bar{R}_{\tilde{A}}/\bar{R}_{\tilde{B}}$ distribution was shown to have two distinct peaks, the 2D signature at $\bar{R}_{\tilde{A}}/\bar{R}_{\tilde{B}} = 1.2079$ ($\bar{R}_{\tilde{A}}/\bar{R}_{\tilde{B}} = \ln 4/\ln 3 \simeq 1.262$ for an infinite sheet), and the quasi-1D signature at $\bar{R}_{\tilde{A}}/\bar{R}_{\tilde{B}} = 1.0$. The 2D peak dominated at low grain densities (regardless of the grain boundary resistivity) and at low grain boundary resistivity (regardless of the grain density). The 1D peak, on the other hand, was only found present at moderate grain densities with a high grain boundary resistivity, since going to very high grain densities remarkably showed a re-approach to the 2D signature distribution, suggesting that samples comprised high grain densities relative to the probe pitch will appear more homogeneous to the M4PP.

The Hall effect signals of all three M4PP configurations were found to have similar distributions, although different in magnitude, with the B configuration being the strongest of the three Hall signals overall. All three showed the strongest Hall signal at a high grain boundary resistivity and with moderate grain densities (relative to the probe pitch). This suggests that the Halls signal could in fact be used as a parameter for the qualitative evaluation of the electrical continuity of a 2D material.

Overall, our observations suggest that the best conditions for the qualitative evaluation of the electrical continuity of a given material are achieved by actively adapting the probe pitch to the size of the grains within the measured sample, so that the two become comparable in size, as this provides the best sensitivity to the current transport conditions on the measured sample.

ACKNOWLEDGMENTS

The Danish National Research Foundation has funded the Center for Individual Nanoparticle Functionality, CINF (DNRF54), and this work was financially supported by Innovation Fund Denmark and the Villum Foundation, Project No. VKR023117. We would also like to thank Alberto Cagliani for fruitful discussions.

[1]K. S. Novoselov, A. K. Geim, S. V. Morozov, D. Jiang, Y. Zhang, S. V. Dubonos, I. V. Grigorieva, and A. A. Firsov, Science **306**, 666 (2004).
[2]A. J. Strudwick, N. E. Weber, M. G. Schwab, M. Kettner, R. T. Weitz, J. R. Wu, and K. Mu, ACS Nano **9**, 31 (2015).
[3]G. Deokar, J. Avila, I. Razado-Colambo, J.-L. Codron, C. Boyaval, E. Galopin, M.-C. Asensio, and D. Vignaud, Carbon **89**, 82 (2015).
[4]X. Li, C. W. Magnuson, A. Venugopal, J. An, J. W. Suk, B. Han, M. Borysiak, W. Cai, A. Velamakanni, Y. Zhu, L. Fu, E. M. Vogel, E. Voelkl, L. Colombo, and R. S. Ruoff, Nano Lett. **10**, 4328 (2010).
[5]L. P. Biró and P. Lambin, New J. Phys. **15**, 035024 (2013).
[6]O. V. Yazyev and S. G. Louie, Nat. Mater. **9**, 806 (2010).
[7]D. V. Tuan, J. Kotakoski, T. Louvet, F. Ortmann, J. C. Meyer, and S. Roche, Nano Lett. **13**, 1730 (2013).
[8]K. W. Clark, X.-G. Zhang, I. V. Vlassiouk, G. He, R. M. Feenstra, and A.-P. Li, ACS Nano **7**, 7956 (2013).
[9]A. W. Cummings, D. L. Duong, V. L. Nguyen, D. Van Tuan, J. Kotakoski, J. E. Barrios Vargas, Y. H. Lee, and S. Roche, Adv. Mater. **26**, 5079 (2014).
[10]P. Y. Huang, C. S. Ruiz-Vargas, A. M. van der Zande, W. S. Whitney, M. P. Levendorf, J. W. Kevek, S. Garg, J. S. Alden, C. J. Hustedt, Y. Zhu, J. Park, P. L. McEuen, and D. A. Muller, Nature **469**, 389 (2011).
[11]Q. Yu, L. A. Jauregui, W. Wu, R. Colby, J. Tian, Z. Su, H. Cao, Z. Liu, D. Pandey, D. Wei, T. F. Chung, P. Peng, N. P. Guisinger, E. A. Stach, J. Bao, S.-S. Pei, and Y. P. Chen, Nat. Mater. **10**, 443 (2011).
[12]L. A. Jauregui, H. Cao, W. Wu, Q. Yu, and Y. P. Chen, Solid State Commun. **151**, 1100 (2011).
[13]D. Jiménez, A. W. Cummings, F. Chaves, D. Van Tuan, J. Kotakoski, and S. Roche, Appl. Phys. Lett. **104**, 043509 (2014).
[14]M. B. Klarskov, H. F. Dam, D. H. Petersen, T. M. Hansen, A. Löwenborg, T. J. Booth, M. S. Schmidt, R. Lin, P. F. Nielsen, and P. Bøggild, Nanotechnology **22**, 445702 (2011).
[15]J. D. Buron, D. H. Petersen, P. Bøggild, D. G. Cooke, M. Hilke, J. Sun, E. Whiteway, P. F. Nielsen, O. Hansen, A. Yurgens, and P. U. Jepsen, Nano Lett. **12**, 5074 (2012).
[16]J. D. Buron, F. Pizzocchero, B. S. Jessen, T. J. Booth, P. F. Nielsen, O. Hansen, M. Hilke, E. Whiteway, P. U. Jepsen, P. Bøggild, and D. H. Petersen, Nano Lett. **14**, 6348 (2014).
[17]D. H. Petersen, O. Hansen, R. Lin, and P. F. Nielsen, J. Appl. Phys. **104**, 013710 (2008).
[18]M. R. Lotz, M. Boll, O. Hansen, D. Kjær, P. Bøggild, and D. H. Petersen, Appl. Phys. Lett. **105**, 053115 (2014).
[19]M. Boll, M. R. Lotz, O. Hansen, F. Wang, D. Kjær, P. Bøggild, and D. H. Petersen, Phys. Rev. B **90**, 245432 (2014).
[20]R. Rymaszewski, J. Phys. E **2**, 170 (1969).
[21]F. Aurenhammer, R. Klein, and D.-T. Lee, *Voronoi Diagrams and Delaunay Triangulations*, 1st ed. (World Scientific Publishing Co., Inc., River Edge, NJ, 2013).
[22]S. Thorsteinsson, F. Wang, D. H. Petersen, T. M. Hansen, D. Kjær, R. Lin, J. Y. Kim, P. F. Nielsen, and O. Hansen, Rev. Sci. Instrum. **80**, 053902 (2009).
[23]T. Kanagawa, R. Hobara, I. Matsuda, T. Tanikawa, A. Natori, and S. Hasegawa, Phys. Rev. Lett. **91**, 036805 (2003).
[24]I. Kazani, G. De Mey, C. Hertleer, J. Banaszczyk, A. Schwarz, G. Guxho, and L. Van Langenhove, Text. Res. J. **83**, 1587 (2013).